35th AIAA Plasmadynamics and Lasers Conference, Jun 28–Jul 1, Portland Oregon

Numerical Exploration of Flow Control with Glow Discharges

Jonathan Poggie*

Air Force Research Laboratory, Wright-Patterson AFB, OH 45433-7512 USA

A numerical study of glow discharges was carried out in order to evaluate their potential for flow control applications. A three-dimensional computer code has been written to solve the fluid conservation laws, the charged particle continuity equations under the drift-diffusion model, and the Poisson equation in an implicit, loosely-coupled fashion. Preliminary calculations of discharges in nitrogen have been carried out for three configurations: a simple discharge between parallel plates, a discharge between electrodes mounted on a NACA-0012 airfoil in a low-speed flow, and a discharge for a three-dimensional electrode configuration mounted on a flat plate in a hypersonic flow.

I. Introduction

Plasma actuators are currently considered to be a promising means of flow control.[1–7] A number of different plasma generation methods have been considered for flow control schemes, including DC glow discharges, RF glow discharges, and dielectric barrier discharges, and control experiments have been carried out both with and without the presence of an applied magnetic field. Significant control effects have been obtained in experiments for both high-speed[6,7] and low-speed flow.[3,4] Accurate modeling of such flow control devices, however, requires incorporating many physical phenomena which are not incorporated into conventional fluid dynamics models, particularly space charge effects or sheaths.

Over the past few years, a prototype code (PS3D) has been written in order to model flow in the presence of finite space charge effects, and examine the plasma sheaths present near electrode surfaces.[8–12] The current version of the code is three-dimensional, and includes the capability to model the effects of an applied magnetic field. Options are present in the code to model the motion of each species of charged particle using either continuity and momentum equations including particle inertia, or a drift-diffusion equation neglecting particle inertia. Particle inertia is an important factor for the ions in a low-density sheath, but at higher densities, ion inertia can be neglected, as can electron inertia in general for relatively low frequency discharges.

The higher density regime is the focus of the present work, which is aimed at developing a capability to simulate experiments with plasma actuators. Preliminary calculations of DC glow discharges in nitrogen have been carried out for three configurations: a simple discharge between parallel plates, a discharge between electrodes mounted on a NACA-0012 airfoil in a low-speed flow, and a discharge for a three-dimensional electrode configuration mounted on a flat plate in a hypersonic flow.

*Research Aerospace Engineer, AFRL/VAAC, Bldg. 146 Rm. 225, 2210 Eighth St. Associate Fellow AIAA.

II. Methods

A three-dimensional computer code has been written to solve fluid conservation laws, the charged particle continuity equations under the drift-diffusion model, and the Poisson equation in an implicit, loosely-coupled fashion. The physical model and numerical procedure are described in this section.

A. Physical Model

The conservation of mass, momentum, and energy for the overall gas is expressed as:

$$\frac{\partial \rho}{\partial t} + \nabla \cdot (\rho \mathbf{u}) = 0 \tag{1}$$

$$\frac{\partial}{\partial t}(\rho \mathbf{u}) + \nabla \cdot (\rho \mathbf{u}\mathbf{u} - \boldsymbol{\Sigma}) = \zeta \mathbf{E} + \mathbf{j} \times \mathbf{B} \tag{2}$$

$$\frac{\partial \mathcal{E}}{\partial t} + \nabla \cdot (\mathbf{u}\mathcal{E} - \boldsymbol{\Sigma} \cdot \mathbf{u} + \mathbf{Q}) = \mathbf{E} \cdot \mathbf{j} \tag{3}$$

where the total fluid energy is defined as $\mathcal{E} = \rho(\epsilon + \mathbf{u}\cdot\mathbf{u}/2)$. The mass density, the charge density, and the total current density are found by summing over all species: $\rho = \Sigma_s m_s n_s$, $\zeta = \Sigma_s q_s n_s$, and $\mathbf{j} = \Sigma_s q_s n_s \mathbf{v}_s$. The total stress tensor $\boldsymbol{\Sigma}$ is given by the usual constitutive equation for a Newtonian fluid and the heat flux $\mathbf{Q}$ follows Fourier's heat conduction law:

$$\Sigma_{ij} = -p\delta_{ij} + \mu\left(\frac{\partial u_i}{\partial x_j} + \frac{\partial u_j}{\partial x_i}\right) - \frac{2}{3}\mu\frac{\partial u_k}{\partial x_k}\delta_{ij} \tag{4}$$

$$Q_i = -k\frac{\partial T}{\partial x_i} \tag{5}$$

where μ and k are, respectively, the viscosity and thermal conductivity. The transport coefficients were evaluated using the correlations given in Ref. 13.

Neglecting acceleration terms and diffusion due to temperature gradients, the particle and momentum conservation equations for each species can be combined to obtain a drift-diffusion model:

$$\frac{\partial n_s}{\partial t} + \nabla \cdot \{n_s \left[\mathbf{u} + s_s \mu_s \mathbf{M}^s \cdot (\mathbf{E} + \mathbf{u} \times \mathbf{B})\right]\} = \nabla \cdot (D_s \mathbf{M}^s \cdot \nabla n_s) + \omega_s \tag{6}$$

where s_s is the sign of q_s, and the tensor $\mathbf{M}^s$ is defined as:

$$M^s_{ij} = \frac{1}{1 + \mu_s^2 B^2}\left(\delta_{ij} + \mu_s^2 B_i B_j + s_s \mu_s \epsilon_{ijk} B_k\right) \tag{7}$$

The dot product in Eq. (6) corresponds to summation on the second index of M_{ij}. For later use, we define the following terms:

$$\mathbf{V}_s = \mathbf{u} + s_s \mu_s \mathbf{M}^s \cdot (\mathbf{E} + \mathbf{u} \times \mathbf{B}) \tag{8}$$

$$\boldsymbol{\Gamma}_s = n_s s_s \mu_s \mathbf{M}^s \cdot (\mathbf{E} + \mathbf{u} \times \mathbf{B}) - D_s \mathbf{M}^s \cdot \nabla n_s \tag{9}$$

$$\mathbf{w}_s = \boldsymbol{\Gamma}_s / n_s \tag{10}$$

$$\mathbf{v}_s = \mathbf{u} + \mathbf{w}_s \tag{11}$$

These are, respectively, a convection-drift velocity, a species flux relative to the bulk flow, a corresponding species velocity, and a total species velocity.

For the present work, the charged particle generation rate is taken to have the form:

$$\omega_{i,e} = \alpha(E, n)\Gamma_e - \beta n_i n_e \tag{12}$$

where α is the ionization coefficient, β is the recombination coefficient, E is the magnitude of the electric field, Γ_e is the magnitude of the electron flux, and n is the neutral gas number density. All the calculations presented in this paper were carried out for nitrogen gas. Data for the mobilities, diffusion coefficients, ionization coefficient, and recombination coefficient were taken from Ref. 14.

The electric potential is determined from the Poisson equation:

$$\nabla^2 \phi = -\zeta/\epsilon_0 \tag{13}$$

where ϵ_0 is the permittivity of free space, and the electric field is found from $\mathbf{E} = -\nabla\phi$.

Conventional no-slip wall conditions and inlet/outlet boundary conditions were used for the fluid equations. The ion number density was taken to be zero on the anode, and the electron number density on the cathode was found from the relation:

$$\mathbf{\Gamma}_e \cdot \mathbf{n} = -\gamma \mathbf{\Gamma}_i \cdot \mathbf{n} \tag{14}$$

where γ is the secondary emission coefficient, $\mathbf{n}$ is a unit normal vector, and the species fluxes $\mathbf{\Gamma}_{i,e}$ were computed by applying one-sided, second-order spatial differences to Eq. (9). The electron number density at the anode and the ion number density at the cathode were found by extrapolation. The normal derivative of the number densities was set to zero on insulator boundaries.

The potential at the anode was taken to be zero, and the normal component of the electric field was set to zero on the side boundaries. The cathode potential V_c was determined according to the circuit shown in Fig. 1. The corresponding ordinary differential equation is:

$$RC\,\dot{V_c} + V_c = -V + IR \tag{15}$$

where V is the applied voltage, R is the resistance, and I is the total current at the anode predicted by the partial differential equations. The value of the capacitance has no effect on the steady-state solution, and for numerical convenience was taken so that the circuit time constant was $RC = 10\Delta t$, where Δt was the integration time step. Equation (15) was solved using the same discretization as partial differential equations, and the solution was monitored to determine if it had converged to $V_c = -V + IR$.

B. Numerical Methods

The conservation equations (1)–(3) and (6) can be written in the form:

$$\frac{\partial U}{\partial t} + \frac{\partial E}{\partial x} + \frac{\partial F}{\partial y} + \frac{\partial G}{\partial z} = \frac{\partial E_v}{\partial x} + \frac{\partial F_v}{\partial y} + \frac{\partial G_v}{\partial z} + S \tag{16}$$

Applying the standard transformation from physical coordinates (x, y, z) to grid coordinates (ξ, η, ζ), where for example $\overline{U} = U/J$ and $\overline{E} = (\xi_x E + \xi_y F + \xi_z G)/J$, gives:

$$\frac{\partial \overline{U}}{\partial t} + \frac{\partial \overline{E}}{\partial \xi} + \frac{\partial \overline{F}}{\partial \eta} + \frac{\partial \overline{G}}{\partial \zeta} = \frac{\partial \overline{E}_v}{\partial \xi} + \frac{\partial \overline{F}_v}{\partial \eta} + \frac{\partial \overline{G}_v}{\partial \zeta} + \overline{S} \tag{17}$$

Writing Eq. (17) as $\partial\overline{U}/\partial t = R$, and discretizing in time, we have:

$$(1+\theta)\overline{U}^{n+1} - (1+2\theta)\overline{U}^{n} + \theta\overline{U}^{n-1} = \Delta t R^{n+1} \tag{18}$$

where $\theta = 0$ for an implicit Euler scheme and $\theta = 1/2$ for a three point backward scheme. We introduce subiterations such that $\overline{U}^{n+1} \rightarrow \overline{U}^{p+1}$, with $\Delta\overline{U} = \overline{U}^{p+1} - \overline{U}^{p}$. The right hand side R^{n+1} is linearized in the standard 'thin layer' manner. Collecting the implicit terms on the left hand side, and introducing

approximate factoring and a subiteration time step $\Delta\hat{t}$ gives:

$$\begin{aligned}
&\left[I - \frac{\Delta\hat{t}}{1+\theta}(B + \delta_\xi A_1 + \delta_\xi R_1 \delta_\xi + D_{i\xi})\right] \times \\
&\left[I - \frac{\Delta\hat{t}}{1+\theta}(\delta_\eta A_2 + \delta_\eta R_2 \delta_\eta + D_{i\eta})\right] \times \\
&\left[I - \frac{\Delta\hat{t}}{1+\theta}(\delta_\zeta A_3 + \delta_\zeta R_3 \delta_\zeta + D_{i\zeta})\right] \Delta\overline{U} = \\
&- \frac{\Delta\hat{t}}{1+\theta}\left\{\frac{(1+\theta)\overline{U}^p - (1+2\theta)\overline{U}^n + \theta\overline{U}^{n-1}}{\Delta t} - R^p - D_e\overline{U}^p\right\}
\end{aligned} \tag{19}$$

where B is the source Jacobian, and A_{1-3} and R_{1-3} are flux Jacobians.

For the bulk fluid conservation laws, the symbols D_i and D_e are, respectively, the implicit and explicit damping operators described by Pulliam.[15] The explicit damping operator uses a nonlinear blend of second- and fourth-order damping.[16] The spatial derivatives are evaluated using second order central differences.

For the drift-diffusion equations, no damping is used. Instead, these equations are discretized in space using a second-order upwind scheme based on the convection-drift velocity $\mathbf{V}_s$ defined in Eq. (8). The minmod limiter is employed. An upwind method is also applied when calculating the species fluxes present in the source terms. (See the discussion of the charged particle generation term in Ref. 14.)

The Poisson equation is solved using an approximately factored implicit scheme, adapted from the approach described by Holst.[17,18] The three-dimensional Poisson equation (13) can be written in the form:

$$\frac{\partial E}{\partial x} + \frac{\partial F}{\partial y} + \frac{\partial G}{\partial z} = S \tag{20}$$

where $E = \partial\phi/\partial x$, $F = \partial\phi/\partial y$, $G = \partial\phi/\partial z$, and $S = -\zeta/\epsilon_0$. Applying the transformation of coordinates, this becomes:

$$\frac{\partial \overline{E}}{\partial \xi} + \frac{\partial \overline{F}}{\partial \eta} + \frac{\partial \overline{G}}{\partial \zeta} = \overline{S} \tag{21}$$

Following the procedure described by Holst, we introduce an artificial time term:

$$\frac{\partial \phi}{\partial \tau} = L\phi = \frac{\partial \overline{E}}{\partial \xi} + \frac{\partial \overline{F}}{\partial \eta} + \frac{\partial \overline{G}}{\partial \zeta} - \overline{S} \tag{22}$$

and develop a procedure that drives the numerical solution towards $L\phi = 0$. We write $\Delta\phi/\Delta\tau = L\phi^{p+1}$, where $\Delta\phi = \phi^{p+1} - \phi^p$. We then linearize the right hand side using the standard 'thin layer' approach, introduce $\alpha = 1/\Delta\tau$, an over-relaxation parameter ω, and approximate factoring. This gives:

$$\left[1 + \alpha^{-1}(D - \delta_\xi A \delta_\xi)\right]\left[1 - \alpha^{-1}\delta_\eta B \delta_\eta\right]\left[1 - \alpha^{-1}\delta_\zeta C \delta_\zeta\right]\Delta\phi = \omega\alpha^{-1}L\phi^p \tag{23}$$

where D is the source Jacobian and A, B, and C are the flux Jacobians. The spatial derivatives are evaluated using second-order central differences. In order to accelerate convergence, the pseudo-time parameter is varied according to the procedure:

$$\alpha_p = \alpha_H \left(\frac{\alpha_L}{\alpha_H}\right)^{\frac{p-1}{M-1}} \tag{24}$$

where α_L and α_H are the low and high bounds on α_p, and p cycles periodically between 1 and M.

The fluid equations, the drift-diffusion equations, and the Poisson equation are solved in a loosely-coupled fashion inside a subiteration loop in the computer code intended to drive $\Delta\overline{U}$ and $\Delta\phi$ toward zero. Typically three subiterations are employed, with a variable number (typically 10-100) of iterations of the Poisson solver within each subiteration.

For each equation, or set of equations, each factor in the factorized scheme is solved in turn using a tridiagonal (Poisson and drift-diffusion equations) or block tridiagonal (fluid equations) algorithm. In solving for each factor, the computation contains three nested loops over the grid indices i, j, and k. One loop index contains dependencies due to the elimination and back-substitution inherent in the solution method, but two of the loop indices have no dependencies. In the computer code, one of these two indices is moved to the inner loop to promote vectorization and locality of memory references, and the other is moved to the outer loop, and executed across multiple threads using OpenMP commands.[19]

III. Glow Discharge in the Absence of Flow

As an initial verification and exploration exercise, a set of calculations was carried out for a simple glow discharge in nitrogen. A grid of $61 \times 141 \times 5$ points, clustered near the electrodes and the symmetry plane, was used. For these calculations, conditions were selected that are typical for laboratory experiments with DC discharges.[20] The pressure was fixed at 670 Pa (5 torr) everywhere, and a no flow and uniform temperature condition (293 K) was imposed over the whole domain. The value $\gamma = 0.1$ was assumed for the secondary emission coefficient. Uniformity was imposed in the z-direction for all variables. In the external circuit shown in Fig. 1, $V = 2000$ V was the applied voltage and $R = 300$ kΩ was the resistance

Figure 2 shows profiles of selected quantities along the discharge centerline. The cathode is at the left and the anode is at the right. Number density profiles are shown in Fig. 2a. The cathode layer is apparent on the left as a region relatively free of electrons, but with a high ion concentration. In the center is the quasi-neutral ($n_i \approx n_e$) positive column. At right is the anode layer, which, in contrast to the cathode layer, is distinguished by a depletion of ions relative to electrons. The maximum ion number density in the cathode layer is on the order of 2×10^{16} m^{-3} (2×10^{10} cm^{-3}), and the maximum number density in the positive column is about 3×10^{15} m^{-3} for both ions and electrons.

The electric potential and the x-component of the electric field are shown in Fig. 2b. A relatively strong electric field is present in the cathode layer, with a weaker field in the positive column, and a slightly stronger field in the anode layer. The greatest magnitude of the electric field occurs at the cathode; the value is on the order of 4×10^5 V/m (4 kV/cm).

Figure 3 shows contour plots of selected discharge properties. The results illustrate the normal glow behavior: the column of ionized gas carrying the discharge current occupies only a portion of the electrode surfaces. Again, the cathode layer is on the left. It has a characteristic thickness of 1-2 mm and an extent along the cathode surface of about 20 mm, and it is characterized by an ion number density that is an order of magnitude above that in the positive column (Fig. 3a). The anode layer has a similar thickness, but a smaller extent in the transverse direction. The electric potential (Fig. 3c) varies strongly within the column of current in the center of the domain, but approaches a distribution that is almost linear in x near the insulated sidewalls.

IV. Airfoil

A set of computations was carried out for a NACA-0012 airfoil configuration in order to examine the potential of low-speed flow control using glow discharges. As an initial code verification exercise, calculations were carried out for an air flow with a Mach number of $M = 0.2$, a Reynolds number of $\mathrm{Re} = 2500$, and and angle of attack of $\alpha = 1°$. The corresponding dimensional conditions were approximately $p_\infty = 179$ Pa, $T_\infty = 289$ K, $U_\infty = 68$ m/s, and $L_{\mathrm{ref}} = 0.30$ m.

The computational grid consisted of $203 \times 101 \times 5$ points, and is illustrated in Fig. 4. An 'O-grid' topology was chosen, with a region of five point overlap on the upstream side of the airfoil. The main plot shows the overall grid, and the inset shows an enlarged view of the airfoil. Note that the grid is highly clustered to resolve the viscous boundary layer near the airfoil surface. Uniformity was imposed along the z-direction.

The pressure coefficient on the airfoil surface is shown in Fig. 5. The higher pressures correspond to the

lower surface of the airfoil. The results of the present calculations using the PS3D code are indicated by a solid line, whereas the symbols represent results obtained for the same grid and flow conditions using a different code (This code, FDL3DI, is a widely used and well tested viscous flow solver.[21]) The agreement between the codes is seen to be extremely close, lending confidence that the PS3D code is correctly implemented.

A second set of calculations was carried out for a nitrogen flow on the same computational grid (Fig. 4). For this case, dimensional freestream conditions were taken to be the same as those in the air flow, so there was a slight difference in the nondimensional conditions from the verification case. The Mach number changed to 0.197 and the Reynolds number to 2494.

Figure 6 shows the basic flowfield for the nitrogen case. The pressure distribution is shown in Fig. 6a. The contour interval is 0.5 Pa. Due to the small angle of attack, only a slight asymmetry exists between the pressure at the top and bottom of the airfoil. A peak pressure of about 184 Pa occurs near the nose of the airfoil, whereas a minimum pressure of about 176 Pa occurs on the front upper surface.

The distribution of the streamwise (u) component of velocity is shown in Fig. 6b. The maximum velocity is about 78 m/s and occurs on the front upper surface of the airfoil. Lower speeds occur in the viscous boundary layer and wake, evident near the airfoil surface and in the flow downstream.

A glow discharge between two electrodes on the upper airfoil surface was investigated. The cathode was located in the region 0.06 m $\leq x \leq$ 0.09 m, and the anode in 0.12 m $\leq x \leq$ 0.15 m. A fixed potential of -500 V was applied at the cathode, and the secondary emission coefficient was taken to be 0.1.

For these calculations, the momentum and energy source terms in Eqs. (2) and (3) were neglected, so that the bulk flow influenced the ionized species, but there was no heating in or force on the bulk gas flow. These assumptions allowed the computations to be completed quickly, but precluded the study of the flow control applications of the discharge.

The ion number density is shown in Fig. 7a. The peak ion concentration occurs just downstream of the cathode. As seen in the case of a glow discharge without flow (Fig. 3), another peak in the ion concentration occurs slightly above the cathode surface. The electron number density is shown in Fig. 7b. Electron concentrations above the cathode are relatively low, but peak just downstream. This region is quasi-neutral. A contour plot of the electric potential is shown in Fig. 7c. Note the large potential gradients near the electrode / insulator juncture at the downstream side of the cathode.

V. Flat Plate

Computations were carried out for a configuration similar to that investigated experimentally by Kimmel *et al.*[6] The freestream velocity was taken to be 688 m/s, the static temperature there was 43 K, and the static pressure was 64 Pa. The working gas was nitrogen, and fluid flow boundary conditions on the plate were an adiabatic, no-slip wall. A fixed potential of -500 V was applied at the cathode, and the secondary emission coefficient was taken to be 0.1. As with the airfoil flow, the glow discharge was decoupled from the bulk gas flow computation: the flow affected the discharge, but the discharge did not affect the flow. Further, the higher temperatures observed in the experiments at the electrode surfaces were neglected for the present preliminary computation.

The computational grid is shown in Fig. 8a. The figure is oriented to display the underside of the flat plate. The grid consisted of $101 \times 81 \times 81$ points, distributed over a 66 mm by 25 mm by 38.1 mm domain. The electrodes have a square shape, and are present in the surface of the plate ($y = 0$ m). They do not extend to the computational boundaries. The cathode is located in the region 0.015 m $\leq x \leq$ 0.025 m, 0.01 m $\leq z \leq$ 0.03 m, and the anode lies in 0.045 m $\leq x \leq$ 0.055 m, 0.01 m $\leq z \leq$ 0.03 m. Grid point clustering is employed at the edges of the electrodes.

A plot of the electric potential on the surface of the computational domain is shown in Fig. 8b. Note that the data are oriented to display the underside of the flat plate. The electrodes are evident as constant potential patches in the solution for the electric potential. The clustering of the potential contours at the edges of the electrodes indicates that the electric field has its greatest magnitude in that region.

An isosurface of the ion number density is shown in Fig. 8c, and a corresponding surface for the electron

number density is presented in Fig. 8d. High levels of the ion concentration are observed above the cathode surface and just upstream of the anode. High electron concentrations are seen only near the anode.

Temperature contours are shown for the symmetry plane in Fig. 9a. The temperature boundary layer is evident as the region of strong temperature gradients near the plate surface. The diagonal contour extending from lower left to upper right in the plot represents the shock generated by hypersonic viscous interaction: the growth of the boundary layer displacement thickness is sufficiently rapid to perturb the inviscid outer flow. Note that these results do not reflect the heating effects of the discharge current. Ongoing work (not shown) indicates that a quite substantial temperature rise is present with the presence of current flow.

The distribution of the electric potential in the symmetry plane is shown in Fig. 9b. The greatest potential variation occurs above the cathode. The ion and electron number density distributions in the symmetry plane are shown in Figs. 9c-d. A quasi-neutral region of relatively high ionization is seen to occur just upstream of the anode. Just above the cathode, the ion number density peaks, but the electron number density is low. A maximum in the charged particle density is observed experimentally in the same region.[6] Quantitative comparision with experiment will be made for ongoing calculations that include the thermal and force effects of the discharge on the flow.

VI. Summary

A progress report has been presented on a program aimed at developing a capability to simulate experiments with plasma actuators. A three-dimensional computer code has been written to solve the fluid conservation laws, the charged particle continuity equations under the drift-diffusion model, and the Poisson equation in an implicit, loosely-coupled fashion. Several numerical techniques, including proper evaluation of source terms and implicit procedures, were critical to successful, high-fidelity simulations (see Sec. II.B).

Preliminary calculations of DC glow discharges in nitrogen flow have been carried out for three configurations: a simple discharge between parallel plates, a discharge between electrodes mounted on a NACA-0012 airfoil in a low-speed flow, and a discharge for a three-dimensional electrode configuration mounted on a flat plate in a hypersonic flow. The cases with the presence of flow display features in common with classic DC discharges. In particular, a peak in the ion number density that was observed near the cathode was an order of magnitude larger than the corresponding density in the quasi-neutral positive column. This result is consistent with experimental observations of DC discharges in high-speed crossflow. Relatively high values of the electric field were observed at electrode/insulator junctures. Adequate grid resolution and a robust numerical scheme were found to be necessary to accurately capture this phenomenon.

In ongoing work, calculations are being carried out that include thermal and body force effects of the discharge on the flow. Including these effects will allow the possibilities of flow control with DC glow discharges to be evaluated, and also allow realistic comparison with experimental data. Preliminary results indicate that, for conditions similar to those examined in the present work, the electric body force does not have a great effect on the neutral gas flow, but heating effects are quite substantial.

Acknowledgments

This project is sponsored by the Air Force Office of Scientific Research, monitored by Dr. J. Schmisseur and Dr. F. Fahroo. A grant of High Performance Computing time was provided by the Department of Defense Major Shared Resource Center at the Engineer Research and Development Center (ERDC). Dr. A. Minga of Cray, Inc. provided assistance in porting the PS3D code to the Cray X1.

References

[1]Bychkov, V., Kuz'min, G., Minaev, I., Rukhadze, A., and Timofeev, I., "Sliding Discharge Application in Aerodynamics," AIAA Paper 2003-0530, January 2003.

[2]Enloe, C. L., McLaughlin, T. E., VanDyken, R. D., Kachner, K. D., Jumper, E. J., and Corke, T. C., "Mechanisms and

Responses of a Single Dielectric Barrier Plasma," AIAA Paper 2003-1021, January 2003.

[3]Post, M. L. and Corke, T. C., "Separation Control on High Angle of Attack Airfoil Using Plasma Actuators," AIAA Paper 2003-1024, January 2003.

[4]Roth, J. R., Sin, H., Madhan, R. C. M., and Wilkinson, S. P., "Flow Re-attachment and Acceleration by Paraelectric and Peristaltic Electrohydrodynamic (EHD) Effects," AIAA Paper 2003-0531, January 2003.

[5]Wilkinson, S. P., "Investigation of an Oscillating Surface Plasma for Turbulent Drag Reduction," AIAA Paper 2003-1023, January 2003.

[6]Kimmel, R. L., Hayes, J. R., Menart, J. A., and Shang, J., "Effect of Surface Plasma Discharges on Boundary Layers at Mach 5," AIAA Paper 2004-0509, January 2004.

[7]Meyer, R., Chintala, N., Bystricky, B., Hicks, A., Cundy, M., Lempert, W. R., and Adamovich, I. V., "Lorentz Force Effect on a Supersonic Ionized Boundary Layer," AIAA Paper 2004-0510, American Institute of Aeronautics and Astronautics, January 2004.

[8]Poggie, J. and Gaitonde, D. V., "Electrode Boundary Conditions in Magnetogasdynamic Flow Control," AIAA Paper 2002-0199, January 2002.

[9]Poggie, J., Gaitonde, D. V., and Sternberg, N., "Numerical Simulation of Plasma Sheaths in Aerodynamic Applications," AIAA Paper 2002-2166, May 2002.

[10]Poggie, J., "Numerical Simulation of Electromagnetic Flow Control for Hypersonic Systems," AIAA Paper 2002-5182, October 2002.

[11]Poggie, J. and Sternberg, N., "Numerical Simulation of Electrode Sheaths in a Magnetized Plasma," AIAA Paper 2003-0359, January 2003.

[12]Poggie, J. and Sternberg, N., "Numerical Simulation of Glow Discharges for High-Speed Flow Control," AIAA Paper 2004-0177, January 2004.

[13]White, F. M., *Viscous Fluid Flow*, McGraw-Hill, New York, 2nd ed., 1991.

[14]Surzhikov, S. T. and Shang, J. S., "Two-Component Plasma Model for Two-Dimensional Glow Discharge in Magnetic Field," *Journal of Computational Physics*, 2004, In press.

[15]Pulliam, T. H., "Implicit Finite-Difference Simulations of Three-Dimensional Compressible Flow," *AIAA Journal*, Vol. 18, No. 2, 1980, pp. 159–167.

[16]Jameson, A., Schmidt, W., and Turkel, E., "Numerical Solutions of the Euler Equations by a Finite Volume Method Using Runge-Kutta Time Stepping Schemes," AIAA Paper 81-1259, 1981.

[17]Holst, T. L., "On Approximate Factorization Schemes for Solving the Full Potential Equation," NASA TM 110435, National Aeronautics and Space Administration, 1997.

[18]Holst, T. L., "Transonic Flow Computations Using Nonlinear Potential Methods," *Progress in Aerospace Sciences*, Vol. 36, 2000, pp. 1–61.

[19]Chandra, R., Dagum, L., Kohr, D., Maydan, D., McDonald, J., and Menon, R., *Parallel Programming in OpenMP*, Academic Press, San Diego, 2001.

[20]Lieberman, M. A. and Lichtenberg, A. J., *Principles of Plasma Discharges and Materials Processing*, J. Wiley, New York, 1994.

[21]Rizzetta, D. P. and Visbal, M. R., "Application of Large-Eddy Simulation to Supersonic Compression Ramps," *AIAA Journal*, Vol. 40, No. 8, 2002, pp. 1574–1581.

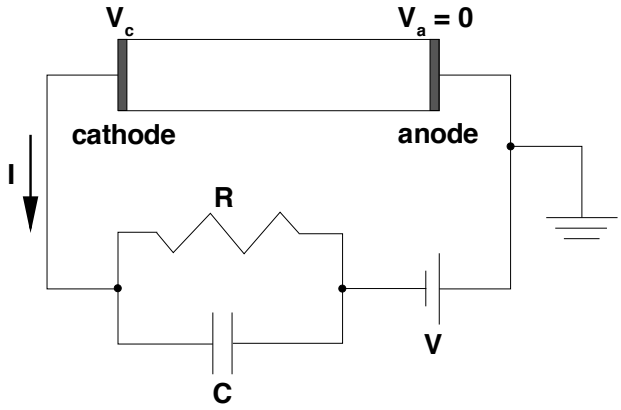

Figure 1. Circuit diagram of glow discharge.

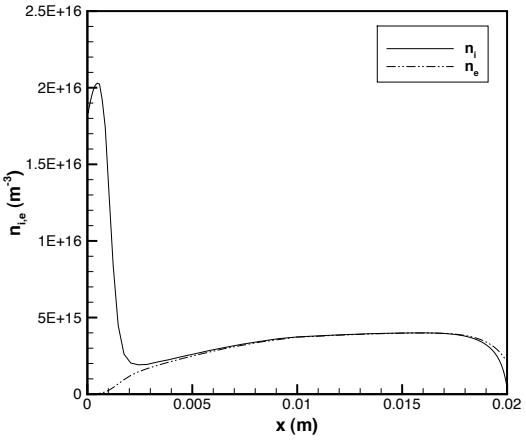

(a) Number densities.

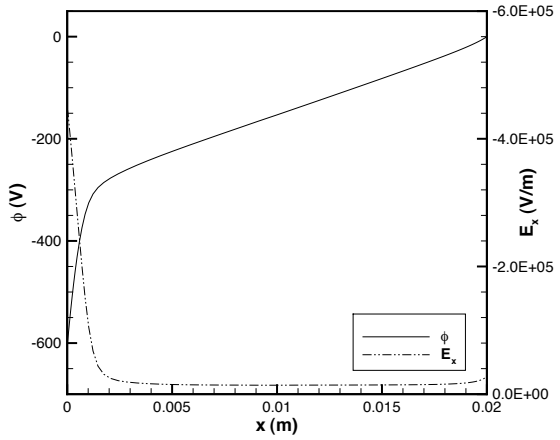

(b) Potential and electric field.

Figure 2. Profiles of selected quantities along the discharge centerline. Discharge conditions: $p = 670$ Pa (5 torr), $V = 2$ kV, $R = 300$ kΩ.

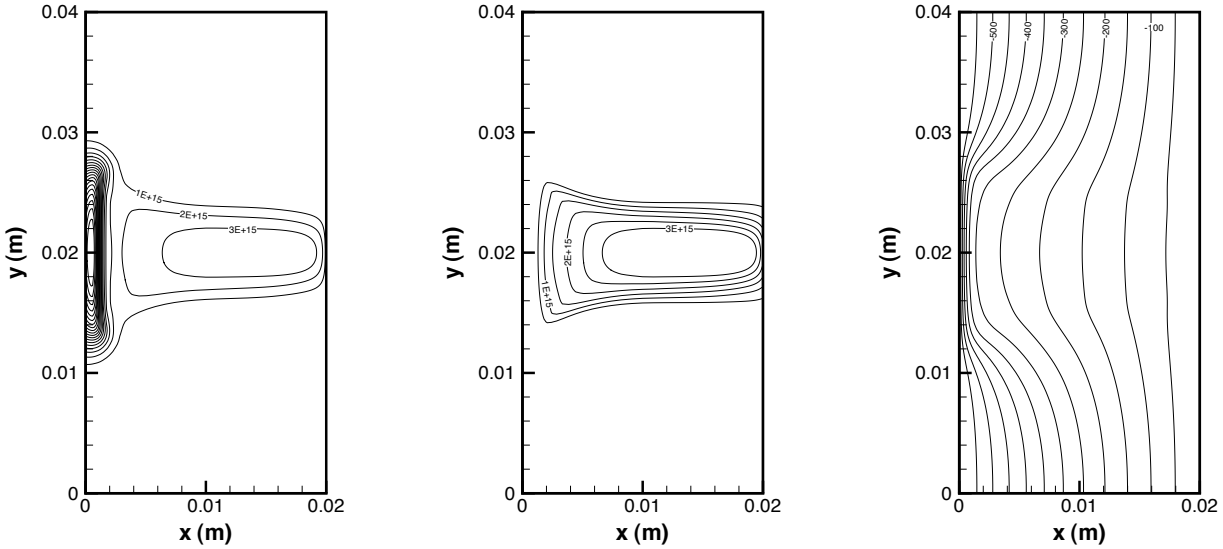

(a) Ion number density.

(b) Electron number density.

(c) Potential.

Figure 3. Contour plots of selected discharge properties. Discharge conditions: $p = 670$ Pa (5 torr), $V = 2$ kV, $R = 300$ kΩ.

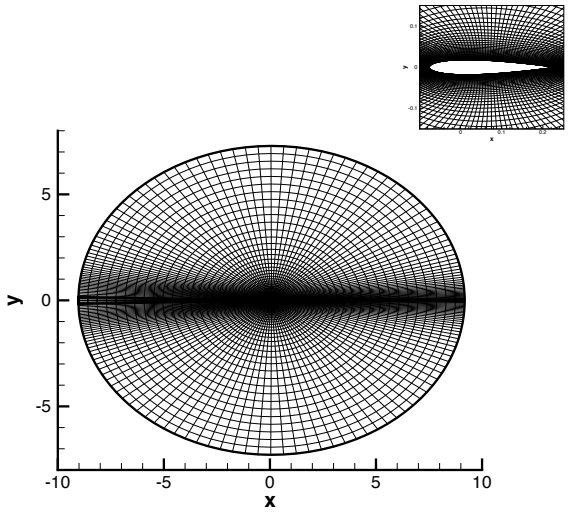

Figure 4. Grid used for airfoil calculations, $203 \times 101 \times 5$ **points.**

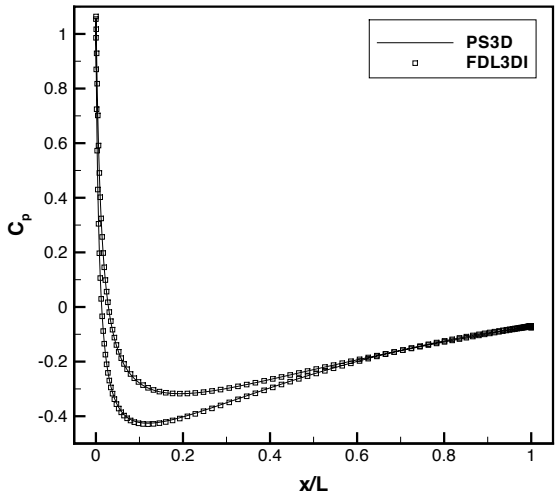

Figure 5. Computed pressure coefficient on airfoil surface: results for PS3D and FDL3DI codes. Air flow, $\mathrm{Ma} = 0.2$**,** $\mathrm{Re} = 2500$**,** $\alpha = 1°$**.**

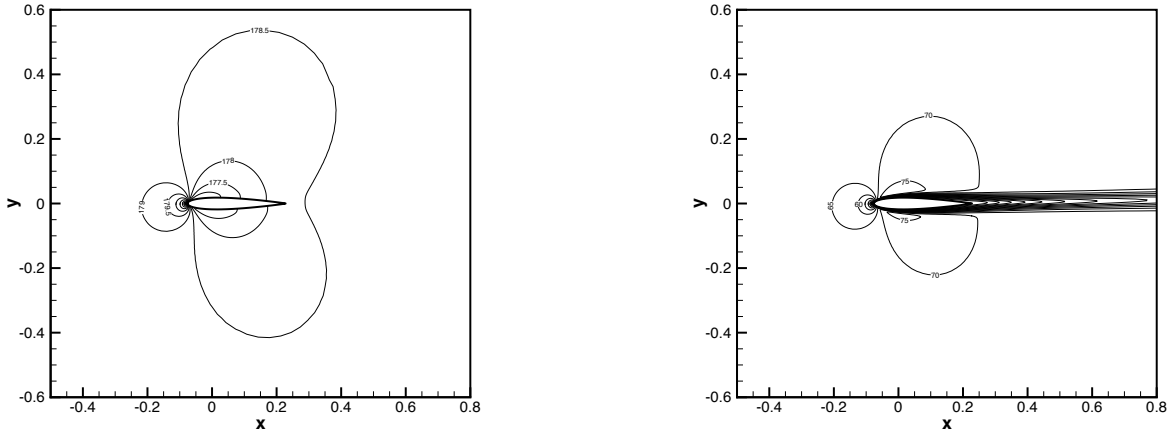

(a) Pressure.

(b) Streamwise velocity.

Figure 6. Airfoil flow, in nitrogen, $\mathrm{Ma} = 0.197$**,** $\mathrm{Re} = 2494$**,** $\alpha = 1°$**.**

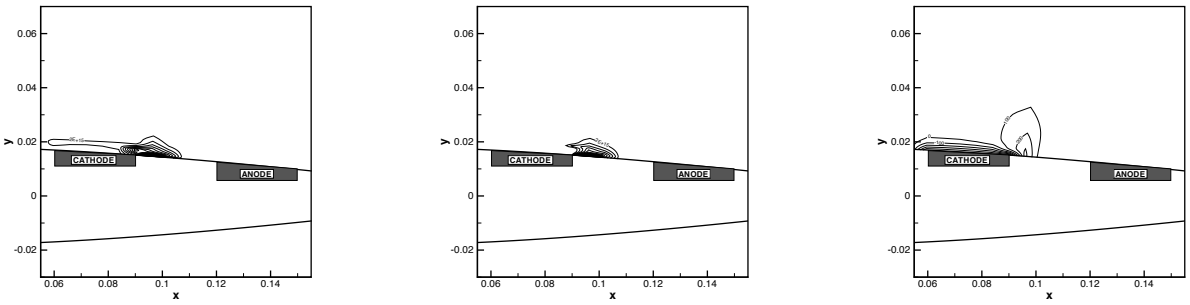

(a) Ion number density.

(b) Electron number density.

(c) Electric potential.

Figure 7. Discharge characteristics for nitrogen flow over airfoil. Cathode potential -500 **V.**

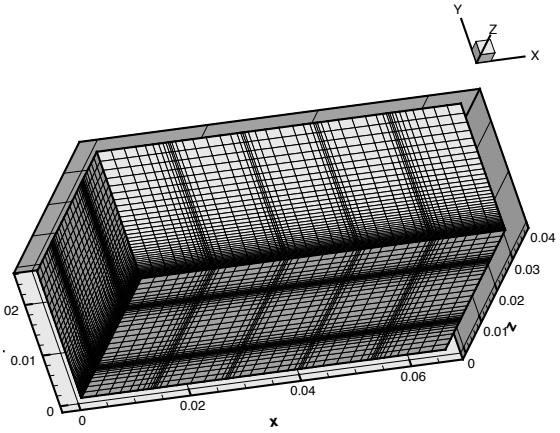

(a) Computational grid.

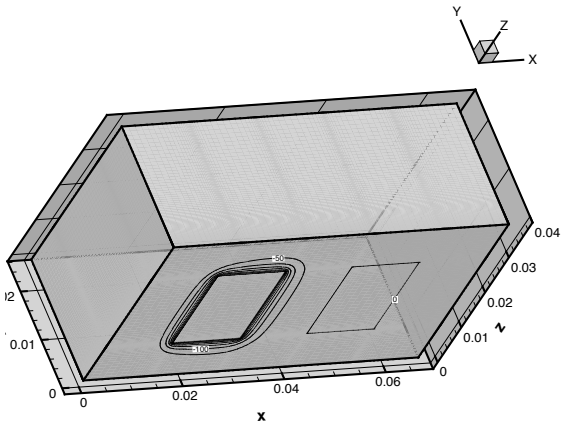

(b) Electric Potential.

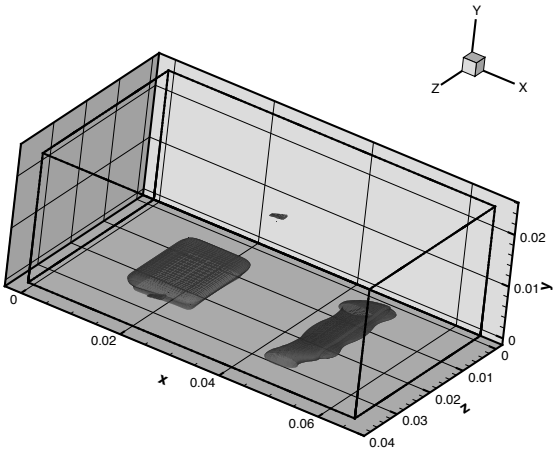

(c) Ion number density, $n_i = 1.6 \times 10^{15}$ m^{-3}.

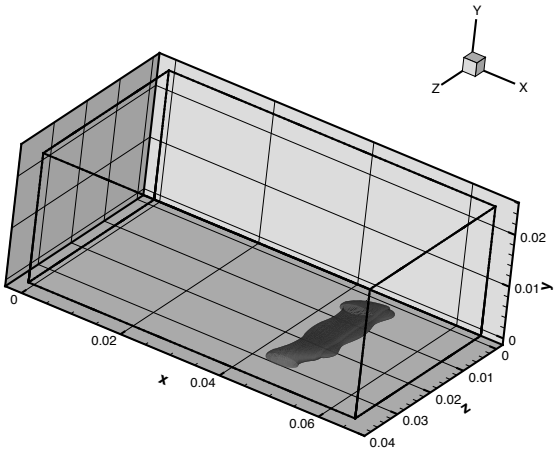

(d) Electron number density, $n_e = 1.6 \times 10^{15}$ m^{-3}.

Figure 8. Three-dimensional computation of Mach 5 flow over flat plate. Conditions: $p_\infty = 64$ Pa, $T_\infty = 43$ K, -500 V applied at cathode.

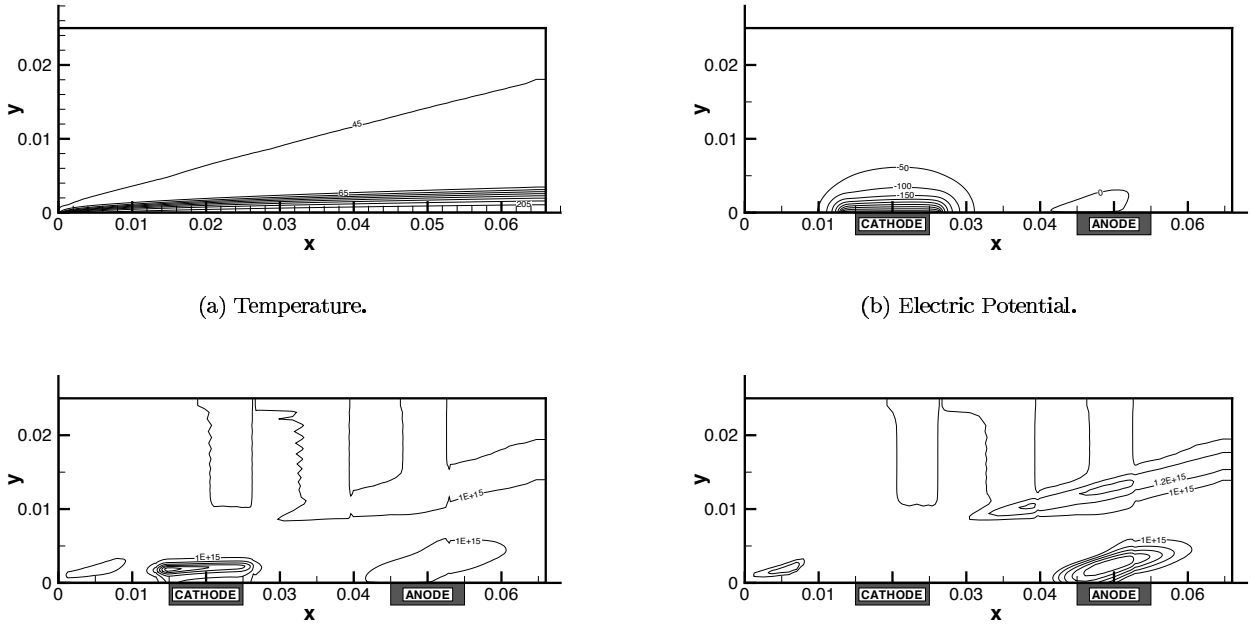

(a) Temperature.

(b) Electric Potential.

(c) Ion number density.

(d) Electron number density.

Figure 9. Results of flat plate computation, symmetry plane. Conditions: $p_\infty = 64$ Pa, $T_\infty = 43$ K. Cathode potential fixed at -500 V.